



Optimizing of porous silicon alloying process with bimetallic nanoparticles

Alwan M. Alwan¹ · Duaa A. Hashim¹ · Muslim F. Jawad¹

Received: 19 May 2018 / Accepted: 14 July 2018 / Published online: 28 July 2018
© Springer Nature Switzerland AG 2018

Abstract

Bimetallic Ag–Au alloy nanoparticles with a tunable size and composition were synthesized by laser beam power density. A set of Psi substrates with different morphologies fabricated by laser-assisted etching process with laser power density from 10 to 40 mW/cm² was explored as a substrate for materialization bimetallic Ag–Au alloy nanoparticles by a simple immersion plating process of Psi in a mixture of AgNO₃ and HAuCl₄ solutions. The materialization of alloy nanoparticles was confirmed by scanning electron microscopy (SEM), X-ray diffraction (XRD), and energy-dispersive X-ray analysis (EDS). The results showed that the sizes and distribution of Ag–Au alloy nanoparticle sizes were easily well-ordered by changing the surface morphologies of Psi layer. Pore-like structures with different pores shapes: ultra-fine pores, irregular (grotto form), circular, and star full pore shape (gambling pores) with different sizes were prepared by changing the irradiation laser power density. Bimetallic Ag–Au alloy nanoparticles, phases, crystalline size, specific surface area, and growth sites of Ag–Au alloy nanoparticles were significantly influenced by pore shape. The lower nanoparticle size with higher S.S.A was obtained when the laser power intensity was about 30 mW/cm².

Keywords Porous silicon · Morphology · Laser-assisted etching · Bimetallic Ag–Au alloy nanoparticles · Immersion plating process

Introduction

Psi is a complex silicon matrix synthesized by etching process of silicon wafer in a solution having hydrofluoric acid (HF) [1]. As a result of adjusting the etching conditions (etching current density, time, irradiation power density, and wafer doping), the surface morphology, porosity, and the type and the density of hydrogenated bonds Si–H_x ($x = 1, 2, 3$) groups of Psi layer can be well-ordered. Psi is a promising material for chemicals and biosensors [2, 3]. The Si–H_x ($x = 1, 2, 3$) groups and their sites on the surface of Psi are capable of reducing the metallic ions to form metallic nanoparticles deposited on the Psi by a simple immersion process of Psi in aqueous solution of metallic

ions [4]. In various practical properties, the activities of Ag–Au alloy nanoparticles are more efficient than those of the corresponding monometallic Ag–Au NPs, for example, in sensors, the catalysis and surface-enhanced Raman scattering (SERS) [5]. Au presents extraordinary biocompatibility, chemical stability, and easy surface alteration; it is frequently considered to be more appropriate for chemical and biomedical uses, Ag alternatively presents higher plasmonic features in the visible range, and it is much more appropriate for optoelectronics and sensing applications. So, to combine these unique properties, a great deal of attention has been devoted to the production of core shell and alloy bimetallic nanoparticles [6].

This paper aims to study the influences of laser power density and the morphologies of n-type Psi on the formation mechanism of Ag–Au alloy nanoparticles through ion reduction process attaining the best condition and adjusting the alloy nanoparticles. The morphological properties of the resulted Ag–Au NPs involving nano sizes, distribution, and surface area were inspected depending on the X-ray diffraction, SEM, FTIR, and EDS analysis.

✉ Alwan M. Alwan
alkrzsm@yahoo.com

¹ Department of Applied Sciences, University of Technology, Baghdad, Iraq

Experimental part

Chemical materials

Hydrofluoric acid 40%, (HIMEDIA), India, was used as received and diluted through high-purity ethanol 99.9% (SIGMA-ALDRICH, Germany) to form the suitable etching solution of 20% HF. HAuCl₄ (99.98%) and AgNO₃ (Aldrich, 99.99%) were dissolved in triply distilled water (Millipore water) to make solutions of 10⁻³ M, according to the following formula [7]:

$$\text{Molarity} = \frac{W/M.Wt}{V} \quad (1)$$

where W (g) is the weight of the AgNO₃ and HAuCl₄, M Wt (g/mol) is the molecular weight, and V is the volume of the dissolved solution. Lastly, 0.5 M aqueous KOH was used to determine the porosity and layer thickness of Psi layer by using gravimetric measurements.

Porous silicon formation

Bare Psi samples were prepared using one side mirror-like (100)-oriented *n*-type monocrystalline silicon wafer with resistivity (10 Ω/cm²) produced by Okmetic company as a substrate in an etching solution consisting of a 1:1 combination of 48% HF and 99.999% C₂H₅ OH. All samples were rinsed in diluted 10% HF for 10 min to remove the native oxide layer on the Si surface. A set of Psi samples was prepared using laser-assisted etching process with a constant current density of 20 mA/cm² for 20 min, under an irradiation source of (CW) 630-nm laser source at different power densities (10 to 40 mW/cm²). The Psi samples were then washed in water and dried at ambient air; the setup of the etching process is shown in Fig. 1.

Synthesis of bimetallic alloy Ag–Au NP

Bimetallic alloy Ag–Au NPs/Psi heterostructures were prepared by simple immersing process of Psi in a mixture of 10⁻³ M AgNO₃ and HAuCl₄ solutions with a ratio of 1:1 for immersion time of about 3 min at room temperature. The ion reduction process of AuNPs and AgNPs is by the Si–H_x (x = 1, 2, 3) groups of the porous layer. The pathway of the reaction can be expressed as follows [8, 9]:

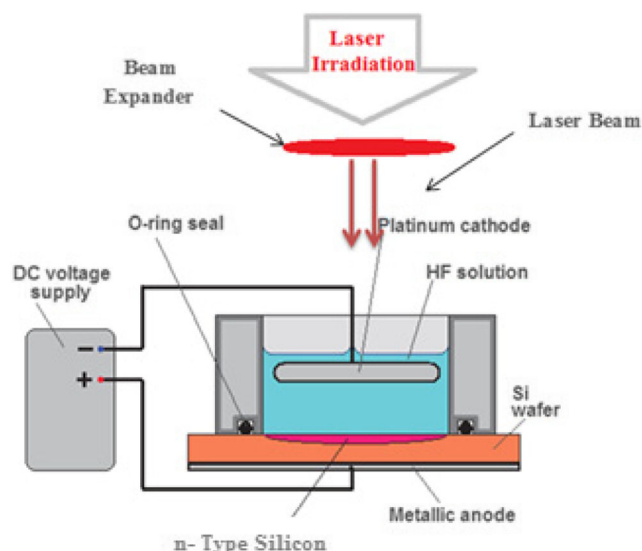


Fig. 1 Setup of laser-assisted etching process

The schematic illustration of the procedures for synthesis of bimetallic alloy Ag–Au NPs/Psi heterostructures is depicted in Fig. 2.

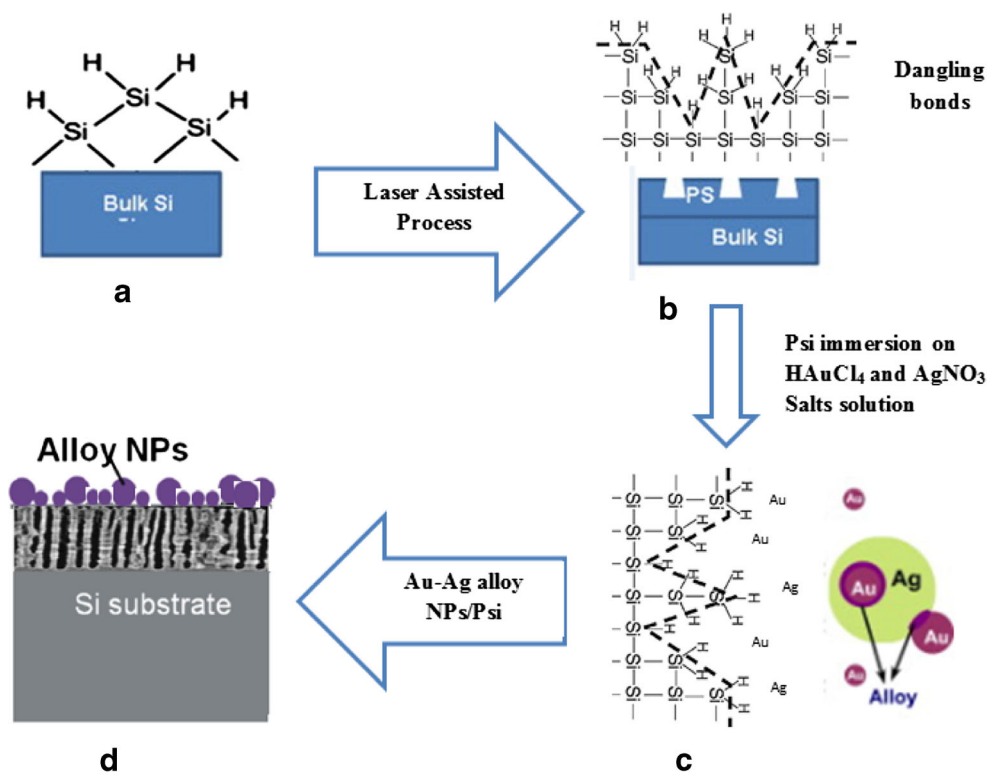
As shown in Fig. 2, one-step method was used to create bimetallic alloy Ag–Au NPs stayed on the Psi in the first step; the monohydride Si–H located onto the bulk Si surface was converted into dihydrides SiH₂ or trihydrides SiH₃ by the etching process and hence a Psi layer was synthesized. After the immersion process of the Psi layer for 3 min in the mixture of AgNO₃ and HAuCl₄ solutions, the Ag–Au NPs/Psi heterostructures were synthesized. As the electronegativity of Ag and Au is greater than that of silicon, the metallic ions Ag⁺ and Au³⁺ in the region of the Psi surface are supposed to capture electrons from the Si. The deposited Au and Ag atoms first form nuclei and then nanoclusters to give AuNPs and AgNPs.

Results and discussion

Morphological features of bare Psi

Porosity and Psi layer are very important factors that describe the surface morphology of Psi layer, which depends on the etching conditions [10] and were calculated by gravimetric method [11]. Porosity of the Psi layers started from 34% at low laser power density (about 10 mW/cm²) and exceeded 76% at high laser power density (about 40 mW/cm²), while the porosity of 20 and 30 mW/cm² was about 65 and 74%, respectively. High laser power densities permit deeper penetration inside the sample and generate pores with larger size. The achieved result is similar to those obtained by other researchers [12, 13]. Figure 3 displays the relation between the Psi layer and the laser power density. In this figure, the Psi layer thickness increases with the increase of the laser power

Fig. 2 Schematic representation of the processes for the synthesis of Psi-stayed bimetallic alloy. **a** Hydrogen passivation covering the bulk Si surface with monohydrides Si–H. **b** Hydrogen covers of Psi surface with dihydrides Si–H₂ or trihydrides Si–H₃. **c** AuNPs and AgNPs in or on the interface of the Psi produced simultaneously by the ion reduction process. **d** A little aggregated AuNPs and AgNPs with more silver-rich alloy and random distribution on Psi support



density. This rise in both porosity and layer thickness with laser power density is due to the increase of the silicon dissolution process that happens as a result of the generation electron-hole couples [12, 13].

The surface morphology (pore form and size distribution) provides very essential structures of bare Psi layer and differs according to the laser power density. Increasing the laser power density changes the topography of the Psi surface, in addition to changing the amounts of dangling bond (growth sites) located on the surface of porous silicon and within the pores

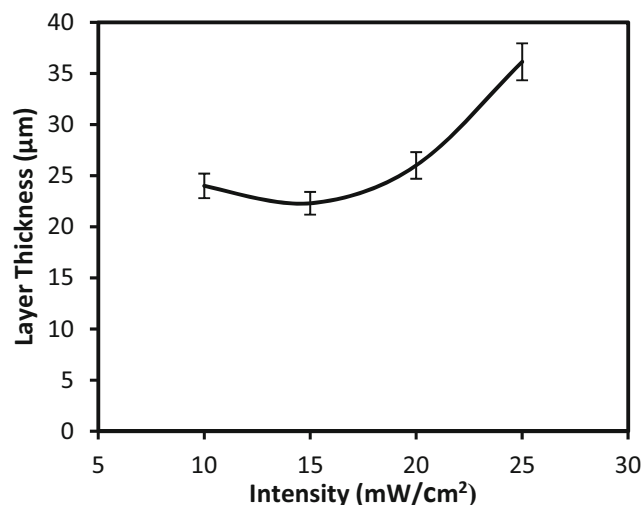
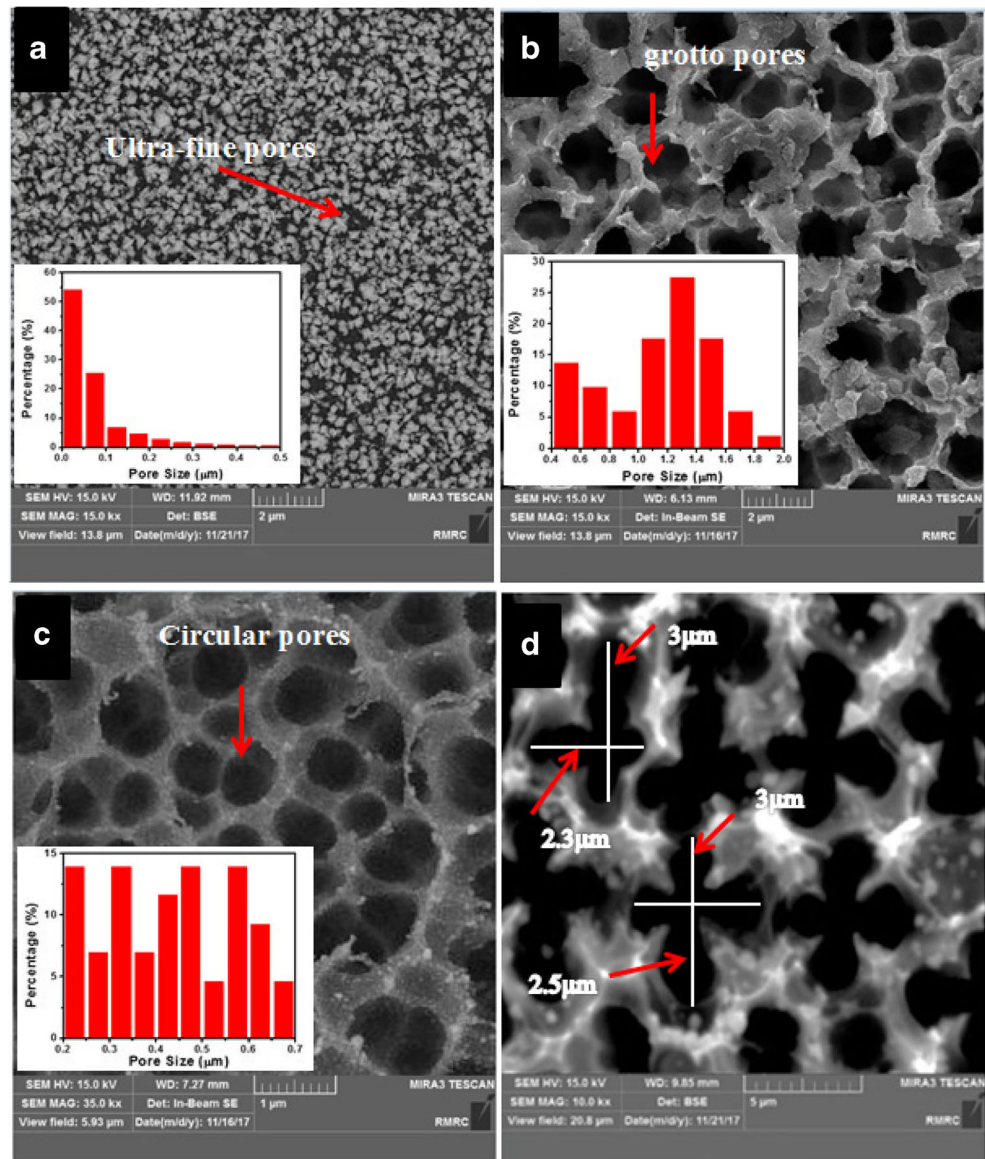


Fig. 3 Psi layer versus of laser power density

inside the porous matrix [14]. These will control the density of ion reduction centers and thus produce a metallic nanoparticle function to laser power density; Fig. 4 reveals the influences of laser power density on the Psi morphology. The SEM images of the bare Psi surface of laser density of 10, 20, 30, and 40 mW/cm² are presented. According to the values of the laser density and the analysis of SEM images, there are four types of macro pore-like structures forms:

1. Formation of ultra-fine pore-like structure. The high density and expanding of the pores led to an overlap in some pores. The pore is ranging from 0.025 to 0.475 μm, and the ultimate of size distribution is about 0.025 μm. The pores are aligned randomly over the surface. This structure was synthesized on the Si surface using low laser power density of about 10 mW/cm².
2. Formation of pore-like structure with irregular shape (nearly grotto form). The pore diameter is ranging from 0.5 to 1.9 μm, and the ultimate of the size distribution is about 1.3 μm. This type of macroporous structure was fabricated on the Si surface using a laser power density of about 20 mW/cm².
3. Formation of pore-like structure with regular shape (nearly circular form) with significant pores overlapping process. This type of macroporous structure was synthesized on the Si surface using a laser power density of about 30 mW/cm². The pore diameter is ranging from 0.225 to 0.675 μm, and the ultimate of the size distribution is about 0.425 μm.

Fig. 4 SEM images of bare macro Psi and statistical pore diameter distributions after irradiation via **a** 10, **b** 20, **c** 30, and **d** 40 mW/cm²



4. Formation of pore-like structure with star full form (nearly like gambling form) due to the high rate of pores overlapping process on the porous surface. The average dimensions of the star full between the opposite points are ranging from 2.65 to 3 μm. This type of macroporous structure was fabricated on the Si surface using higher laser power density of about 40 mW/cm². The charge carrier generation rate G_t owing to the absorption of the incident photon flux (ϕ_{abs}) within the porous layer thickness (L_{Psi}) is given by [15]

$$G_t = \phi_{abs}/L_{Psi} \quad (5)$$

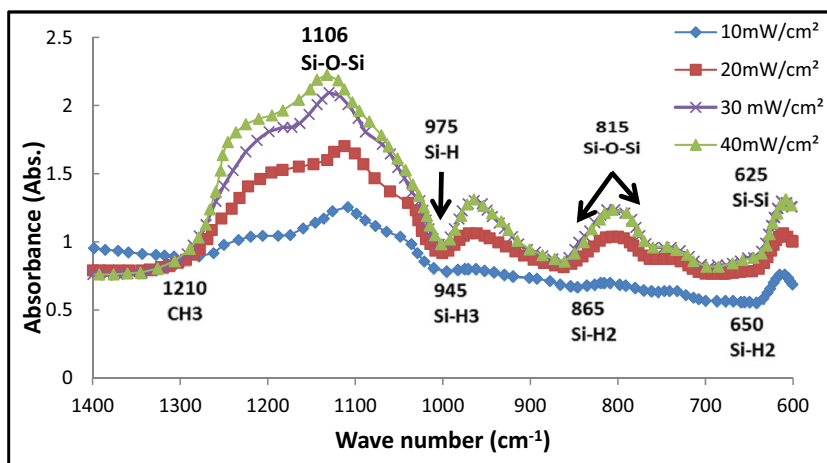
and

$$\phi_{abs} = \phi_{in}(1-R_{psi}) (1-e^{-\alpha L_{psi}}) \quad (6)$$

where ϕ_{abs} is the amount of laser photons absorbed in a porous layer, ϕ_{in} is the incident photon flux, R_{psi} is the reflectivity of the Psi layer, and α is absorption coefficient of Psi layer. Based on Eq. 6, the absorption laser power density rises within the Psi layer and leads to an increase in the porosity on a linear approach. The rise of the porosity and the laser power density will increase the pore size in the Psi matrix. So, the Si dissolution process is a function of the laser power density and reflectivity of the Psi layer. This absorption will enhance the amount of the Si-H_x ($x = 1, 2, 3$) (growth sites), and hence, the Ag and Au ion reduction will take place down in the porous layer itself [16].

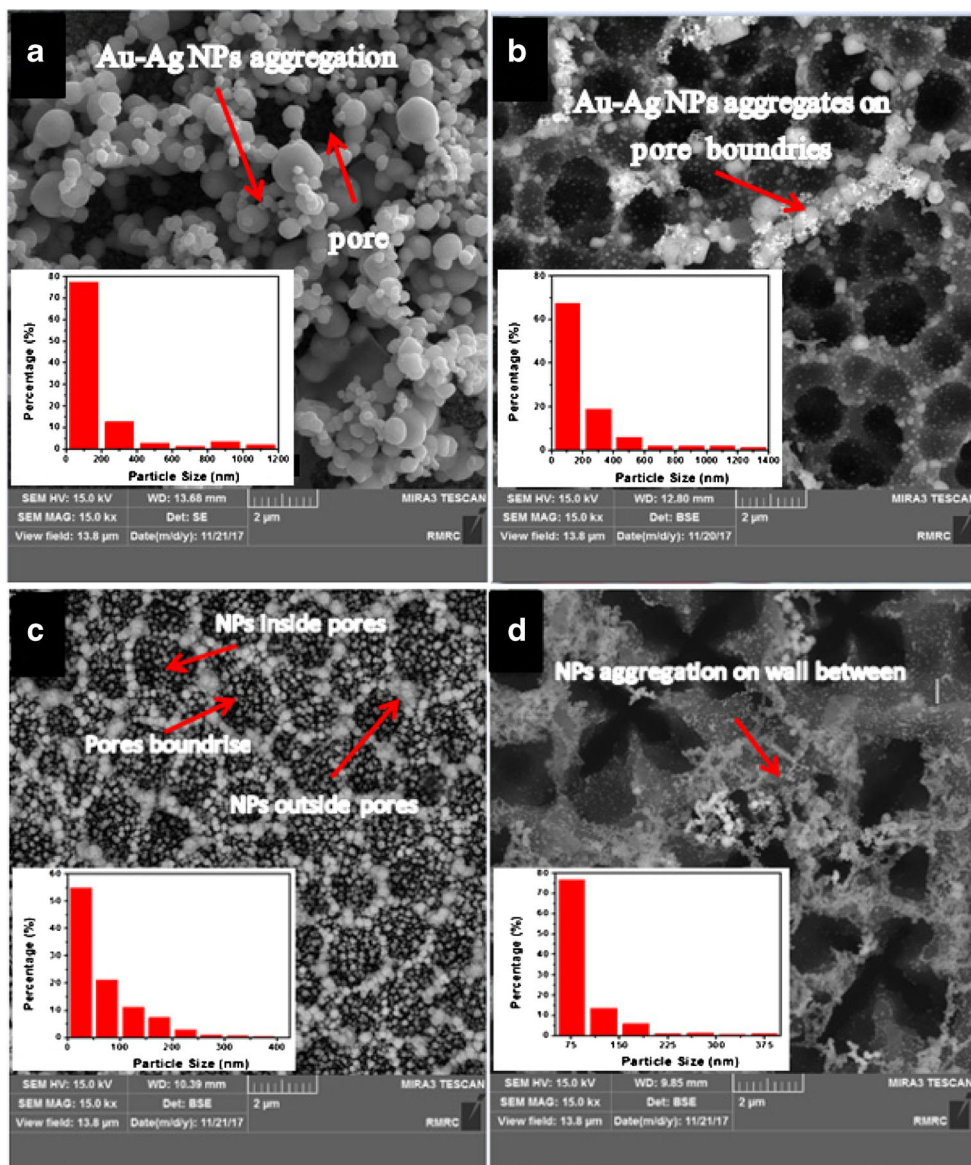
The effects of the laser power density on the chemical species of bare Psi surfaces were determined by FTIR signals from the porous silicon. As shown in Fig. 5, the

Fig. 5 FTIR absorbance spectra of bare Psi after irradiation via **a** 10, **b** 20, **c** 30, and **d** 40 mW/cm²



hydrogen passivation covers the bulk Si surface with monohydride Si–H, dihydride Si–H₂, and trihydride Si–H₃ bonds. The laser power density controls the types of such group and the intensity of the absorption [17].

Fig. 6 SEM images of bimetallic alloy Ag–Au NPs and their statistical particle diameter distributions over Psi after deposition and irradiation via **a** 10, **b** 20, **c** 30, and **d** 40 mW/cm²



Specific peaks are present in the infrared absorption (FTIR) spectra corresponded to monohydrides Si–H; bending mode is located at 975 cm^{-1} , Si–O–Si bond at 1106 cm^{-1} , trihydrides Si–H₃ bond at 945 cm^{-1} mode, and dihydrides Si–H₂ bending between 600 and 800 cm^{-1} [18]. The presence of Si–O–Si bond in all bare Psi samples is due to the natural oxidation process, which occurs owing to the exposure to the ambient air [19]. The spectra of all samples obviously manifested an increase in the absorption of the resulting peaks with the increase of the laser power density.

Morphological features of bimetallic alloy Ag–Au NPs/Psi heterostructures

Modifying the Psi surface features, such as the pore shape and pore size, is one of the significant features for controlling the AuNP and AgNP nanosizes. The topography and the sizes of

bimetallic alloy Ag–Au NPs were found to vary according to the Psi surface features, like the pore size and shape, at the fixed dipping condition [20, 21]. Figure 6 characterizes the surface morphology of bimetallic alloy Ag–Au NP Psi substrates at different laser power densities (10 to 40 mW/cm^2). While, Fig. 7 demonstrates the cross-sectional SEM image of the bimetallic alloy Ag–Au NPs/Psi after deposition as a function of the laser power density.

As shown in Fig. 6, there are three different proposed mechanisms for the materialization of the bimetallic alloy Ag–Au NPs based on Psi morphology. In the ultra-fine pore-like structure, which owns the lowest pore sizes, the aggregated bimetallic alloy Ag–Au NP sizes fluctuated from 100 to 1100 nm and mainly located on the tops of the fine pores in the porous surfaces. The lowest value of the bimetallic alloy Ag–Au NP size is higher than that of the ultra-fine pore sizes, and the highest value of the bimetallic alloy Ag–Au NP size is

Fig. 7 Cross-sectional SEM image of bimetallic alloy Ag–Au NPs/Psi after deposition with laser irradiation via **a** 10, **b** 20, **c** 30, and **d** 40 mW/cm^2

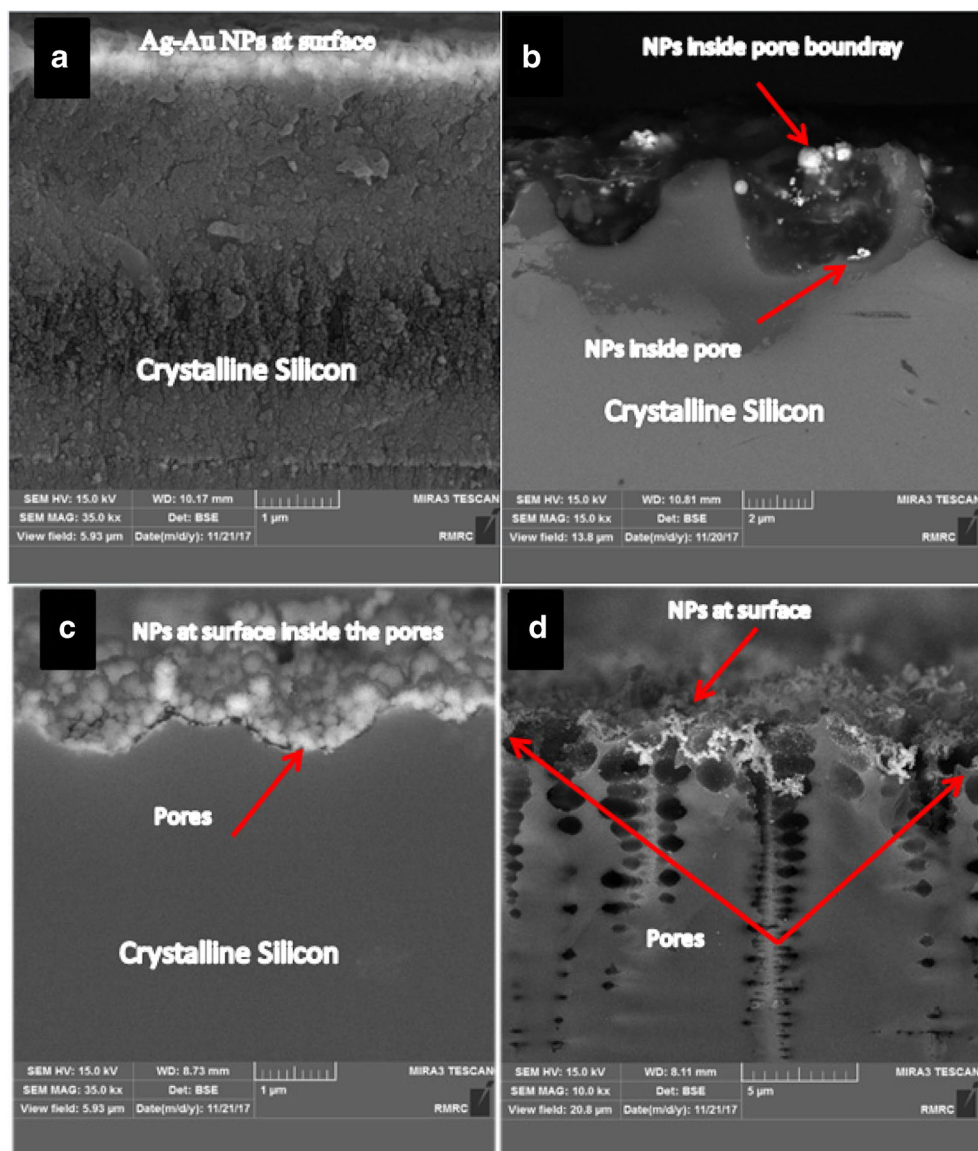
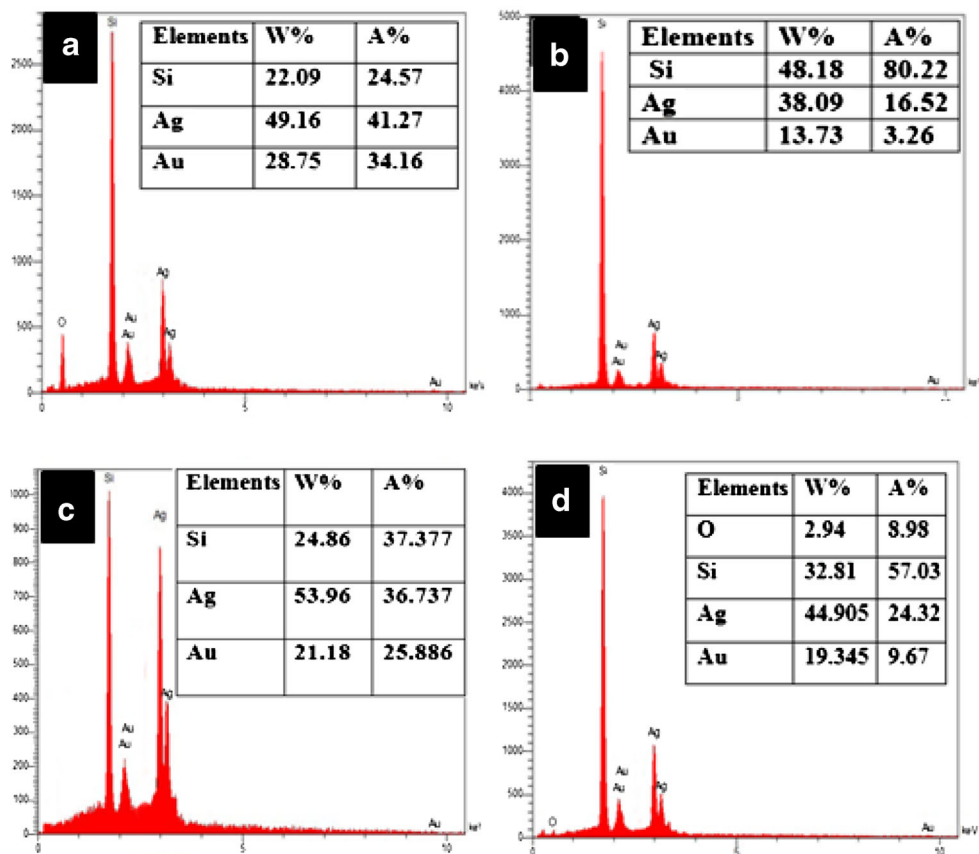


Fig. 8 The EDX spectra of the bimetallic alloy Ag–Au NPs embedded in Psi as a function of irradiated laser power densities via **a** 10, **b** 20, **c** 30, and **d** 40 mW/cm²



higher than that of the biggest value of the pore sizes. Consequently, the density of the bimetallic alloy nano districts is expected to develop (in/out) the ultra-fine pore itself. For pore-like structure with an irregular shape (nearly grotto form)

and a regular shape (nearly circular form), as in Fig. 6b, c, the pore diameter has a large value compared with bimetallic alloy Ag–Au NP size and has a high tendency to enter into the pores. The circular pore shape leads to synthesize bimetallic

Fig. 9 The XRD spectra of the bimetallic alloy Ag–Au NPs embedded in Psi as a function of the irradiated laser power densities via **a** 10, **b** 20, **c** 30, and **d** 40 mW/cm²

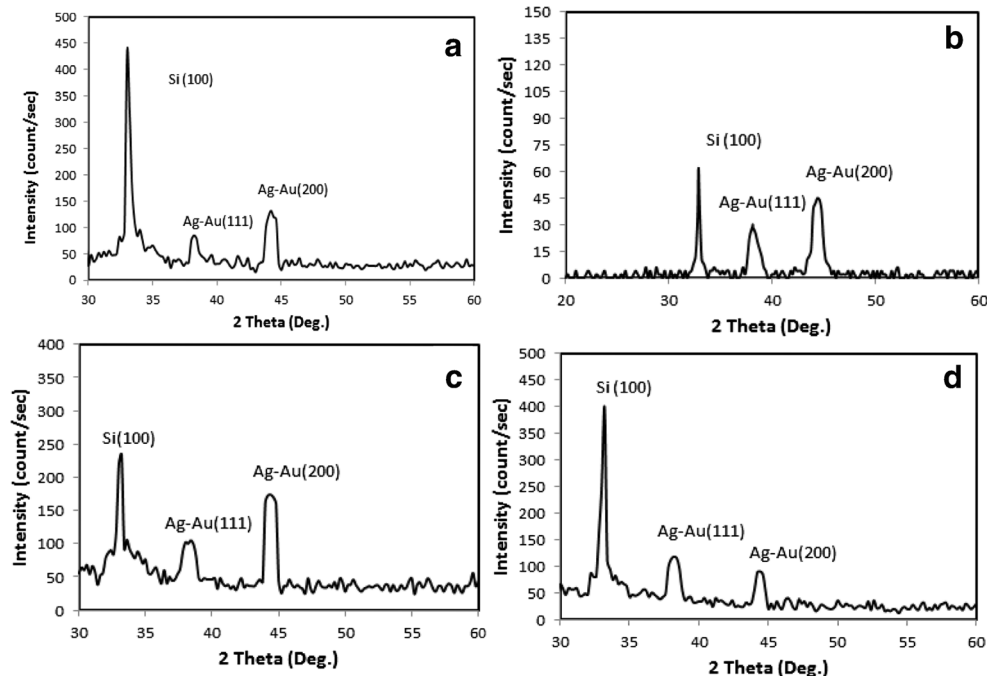


Table 1 Investigational and typical diffraction angles (2θ) of Ag–Au bimetallic alloy nanoparticles in the planes (111) and (200)

Laser Power density (mW/cm ²)	Diffraction angle in (111) 2θ in degree Experimental standard	ASTM (Silver)	ASTM (Gold)	Diffraction angle in (111) 2θ in degree Experimental standard	ASTM (Silver)	ASTM (Gold)
10	38.2			44.2		
20	38.12	38.116	38.184	44	44.277	44.392
30	38.2			44.4		
40	38.2			44.4		

alloy with a high degree of uniformity and isolated spherical seeds distributed over the pore surface compared with that of grotto form pore-like structure, in which the growth of nanoparticles is mainly occurred at the pore boundaries in the aggregated form. The sizes of bimetallic alloy Ag–Au NPs will range from 100 to 1300 nm and 25 to 375 nm for Fig. 6c. Figure 6d manifests that the bimetallic alloy Ag–Au NPs deposited on the silicon surface region and at the outer shell of the pore region. The sizes of bimetallic alloy Ag–Au NPs will range from 75 to 375 nm. These different forms of bimetallic alloy Ag–Au NPs refer to the fact that the metallic deposition process is governed by the amounts of Si–H_x ($x = 1, 2, 3$) (growth sites) and where they produced after the etching process. The surface of silicon regions is fully coated with the monohydrides Si–H while for the porous structures, the types of growth sites are mainly dihydrides Si–H₂ and trihydrides Si–H₃; these are widely located at the inner surface of pores and the tips of silicon nanocrystallites. So, the growth of bimetallic alloy Ag–Au NPs is modified with these different forms.

The EDX spectra of the bimetallic alloy Ag–Au NPs deposited on bare Psi as a function of the laser power density are illustrated in Fig. 8a–d. The EDS analysis confirmed the presence of Au, Ag, and Si elements on the Psi sample. The presence of Si element is due to the Si substrate. As shown from this figure, three specific points can be recognized easily; the intensity of AgNPs peak is higher than that of the AuNPs, the deposition rate of the Ag NPs is higher compared with the AuNPs, and the higher deposition rate of bimetallic alloy Ag–Au NPs is obtained in the porous surface consisting of an ultra-fine pore-like structure compared with the other structures.

X-ray diffraction analysis

The X-ray diffraction analysis of the bimetallic alloy Ag–Au NPs/Psi heterostructures, synthesized by the laser-assisted etching process with different laser power densities of 10 to 40 mW/cm², is depicted in Fig. 9. The bimetallic alloy Ag–Au NP materialization as the result of the metallic ions Ag⁺¹ and Au⁺³ reduction process can be greatly due to the identical

lattice factors of 0.408 and 0.409 nm for Au and Ag, respectively. This small variation in lattice factors being smaller than the amplitude of thermal vibrations of atoms has already been postulated to favor the alloy formation even at the nanometer scale [22]. Bimetallic nanoparticles are very essential as catalysts due to their extraordinary surface-to-volume ratios [23]. Gold and silver have the similar face-centered cubic (FCC) structure and interatomic spacing, and they certainly construct an alloy phase, which has been removed from the introduction [24]. XRD data of bimetallic alloy Ag–Au NPs showed specific diffraction peaks at (38.12) and (44), which can be indexed to (111) and (200) planes of pure Ag and Au (ASTM Standard Card). It approves that Ag and Au are the chief composition of the bimetallic alloy. The investigational and typical diffraction angles of AuNPs and AgNPs at the laser power densities are tabulated in Table 1. In this table, the variation in the diffraction angle (2θ) is owing to the local occurrence of the microscopic deformation (strain) and the overlap of the diffraction peaks of both small and large ones [25, 26].

The reliance of the bimetallic alloy and specific surface area of Ag–Au NPs on the laser power density reveals new features for adjusting the characteristics of the bimetallic Ag–Au NPs. The width of the diffraction peak is influenced by the crystallite sizes, and the big crystallite sizes resulted sharp peaks, while the small size causes wider peaks [25]. The peaks of the bimetallic alloy Ag–Au NP samples are very broad and indicate rather small particle sizes. The Ag–Au NPs size and therefore a higher specific surface area (S.S.A.) were achieved with the smaller

Table 2 The grain size of the Ag–Au bimetallic alloy nanoparticles in the planes (111) and (200)

Laser power density (mW/cm ²)	Size of Ag–Au alloy nanoparticle in (111) plane (nm)	Size of Ag–Au alloy nanoparticles in (200) plane (nm)
10	9.2	8.7
20	7.29	8.1
30	5.36	6.29
40	6.53	8.9

Table 3 The S.S.A of the Ag–Au alloy nanoparticles in the planes (111) and (200)

Laser power density (mW/cm ²)	S.S.A. of Ag–Au alloy nanoparticle in (111) plane (nm)	S.S.A. of Ag–Au alloy nanoparticles in (200) plane (nm)
10	51.7	54.63
20	68.82	62
30	92.91	79.17
40	78.4	55.4

particle sizes. The average bimetallic alloy Ag–Au NP size was calculated by using Scherer's formula [27]:

$$L = \frac{0.9 \lambda}{B \cos \theta} \quad (7)$$

The S.S.A., which is the unique specific value of the nanostructured material, is known as [11]

$$\text{S.S.A.} = \frac{6 \times 10^3}{D * \rho} \quad (8)$$

where ρ is the density of Au and Ag (19.3 and 10.5 g/cm³), respectively, whereas the density of the bimetallic alloy Ag–Au NPs according to the laser power density (10, 20, 30, and 40 mW/cm²) is about 12.624, 11.943, 12.049, and 12.171 g/cm³, respectively. These values can be determined using equation, which depends on the EDS analysis [28, 29]:

$$D = \frac{a * \rho + b * \rho}{a + b} \quad (9)$$

where D: density (g/cm³), a: wt.% Au, and b: wt.%Ag.

Table 2 demonstrates the rise in the grain size of the bimetallic alloy Ag–Au NPs in the plane (111) and (200) on Psi samples when increasing the etching laser power density. The lowest bimetallic alloy Ag–Au NP grain size is about 5.36 nm at 30 mW/cm², while the highest is about 9.2 nm at 10 mW/cm². In Table 3, the lowest S.S.A of the Ag–Au alloy nanoparticles is about 51.7 nm at 10 mW/cm², whereas the highest is about 92.91 nm at 30 mW/cm². This means that the SEM analysis indicates the aggregated nanoparticles. This variation is owing to the point that the bimetallic alloy Ag–Au NP materialization is influenced by the morphology of Psi.

Conclusion

In this work, bimetallic Ag–Au alloy nanoparticles with a tunable size and composition were synthesized using ion reduction process of Au and Ag ions by the dangling bonds of the Psi layer. Four types of pore morphology, ultra-fine pores, irregular (grotto form), circular, and star full pore shape

(gambling form) with different sizes, were synthesized by the laser-assisted etching process. Varying the laser power density changes the morphology of the Psi surface, in addition to changing the amount of dangling bond (growth sites) located on the surface of porous silicon that will control the density of ion reduction centers and thus produce metallic nanoparticles as a function of the laser power density. Bimetallic Ag–Au alloy nanoparticles deposited with a high degree of uniformity and isolated spherical seeds distributed over the pore surface with the size ranging from 25 to 375 nm. Additional works in the use of these new bimetallic Ag–Au NP alloys will open a novel scene in the field of applied nanosciences.

Acknowledgments The authors would like to express their gratitude to the Department of Applied Sciences/University of Technology and Razi metallurgical research center, Iran, for using the SEM (MIRA3 TESCAN) and the EDS analyses.

Publisher's Note Springer Nature remains neutral with regard to jurisdictional claims in published maps and institutional affiliations.

References

- Canham LT (1990) Silicon quantum wire array fabrication by electrochemical and chemical dissolution of wafers. *Appl Phys Lett* 57(10):1046–1048
- Thust M, Schoning MJ, Frohnhoff S, Arens-Fischer R, Kordos P, Luth H (1996) Porous silicon as a substrate materials potentiometric biosensor. *Meas Sci Technol* 7:26
- Schoning MJ, Ronkel F, Crott M, Thust M, Kordos P, Luth H (1997) Miniaturization of potentiometric sensors using porous silicon microtechnology. *Electrochim Acta* 42:20
- Alwan AM, Yousif AA, Wali LA (2017) The growth of the silver nanoparticles on the mesoporous silicon and macroporous silicon: a comparative study. *Indian J Pure Appl Phys* 55:813–820
- Harraz FA, Ismail AA, Bouzid H, Al-Sayari S, Al-Hajry A, Al-Assiris M (2015) Surface-enhanced Raman scattering (SERS)—active substrates from silver plated-porous silicon for detection of crystal violet. *Appl Surf Sci* 331:241–247
- Yang L, Li X, Tuo X, Van Nguyen TT, Luo X, Hong M (2011) Alloy nanoparticle plasmon resonance for enhancing broadband antireflection of laser-textured silicon surfaces. *Opt Express* 19:4
- Alwan, AM, Yousif, AA, Wali, LA (2017) A study on the morphology of the silver nanoparticles deposited on the n-Type porous silicon prepared under different illumination types. *Plasmonics*, pp. 1557–1955
- Alwan AM, Dheyab AB (2017) Room temperature CO₂ gas sensors of AuNPs/mesoPSi hybrid structures. *Appl Nanosci* 7: 335–341
- Jabbar AA, Alwan AM, Haider AJ (2017) Modifying and fine controlling of silver nanoparticle nucleation sites and SERS performance by double silicon etching process. *Plasmonics*
- Lee S, Kim DY (2005) Effect of incoherent light illumination during electrochemical anodization on the formation and the properties of porous Si. *J Korean Phys Soc* 47(5):880–883
- Alwan AM, Hayder AJ, Jabbar AA (2015) Study on morphological and structural properties of silver plating on laser etched silicon. *Surf Coat Technol* 283:22–28

12. Rashid RB, Alwan AM, Dheyab AB (2018) Morphological and electrical properties of gold nanoparticles /macroPorous silicon for CO₂ gas. *59(1A)*:57–66
13. Feng Z, Yu J, Li K, Feng Y, Padmanabhan K, Yang T (2006) Combined optical, surface and nuclear microscopic assessment of porous silicon formed in HF-acetonitrile. *Surf Coat Technol* 200: 3254–3260
14. Hayder AJ, Alwan AM, Jabbar AA (2016) Optimizing of porous silicon morphology for synthesis of silver nanoparticles. *Microporous Mesoporous Mater* 227:152–160
15. Ahmed AM, Alwan AM (2007) Light-induced etching of silicon. *Eng Technol* 25(3)
16. Alwan AM, Wali LA, Yousif AA (2018) Optimization of AgNPs/mesoPS active substrates for ultra-low molecule detection process. *Springer Silicon* 1876–9918
17. Alwan AM (2007) Organic vapors sensor based on dangling bonds of porous silicon. *Eng Technol* 25(8)
18. Abbas RA, Alwan AM, Amer BD (2018) Study the characteristic of planer and sandwich PSi gas sensor (Comparative Study). *Silicon* (2):1876–9918
19. Alwan AM, Abdulrazaq OA (2008) Aging effect on the photosynthesized porous silicon. *Int J Mod Phys B* 22(4):417–422
20. Zhang H, Lv X, Lv C, Jia Z (2012) N-type porous silicon as an efficient surface enhancement Raman scattering substrate. *Opt Eng* 51:099003–1-099003-5
21. Virga A, Rivolo P, Descrovi E, Chiolerio A, Digregorio G, Frascella F (2012) SERS active Ag nanoparticles in mesoporous silicon: detection of organic molecules and peptide–antibody assays. *J Raman Spectrosc* 43:730–736
22. Devarajan S, Vimalan B, Sampath S (2004) Phase transfer of Au–Ag alloy nanoparticles from aqueous medium to an organic solvent: effect of aging of surfactant on the formation of Ag-rich alloy compositions. *J Colloid Interface Sci* 278:126–113
23. Stephen A, Hashmi K, Hutchings GJ (2006) Gold catalysis. *Angew Chem Int Ed* 45:7896–7936
24. Carretin S, Carmen Blanco M, Corma A, Stephen A, Hashmib K (2006) Heterogeneous gold-catalysed synthesis of phenols. *Adv Synth Catal* 348:1283–1288
25. Liu X, Wang A, Li L, Zhanga T, Moub C-Y, Leec J-F (2013) Synthesis of Au–Ag alloy nanoparticles supported on silica gel via galvanic replacement reaction. *Prog Nat Sci Mater Int* 23(3): 317–325
26. Wang YQ, Ma S, Yang QQ, Li XJ (2012) Size-dependent SERS detection of R6G by silver nanoparticles immersion-plated on silicon nanoporous pillar array. *Appl Surf Sci* 258:5881–5885
27. Zanoni R, Righini G, Mattogno G, Schirone L, Sotgiu G, Rallo F (1998) X-ray photoelectron spectroscopy characterization of stain-etched luminescent porous silicon films. *J Lumin* 80:159–162
28. Kraut C, Stern WB (2000) The density of gold-silver-copper alloys and its calculation from the chemical composition. *Gold Bull* 33(2): 52–55
29. Loni A, M. pSiMedica Ltd. (2014), Porous silicon formation by anodization. Springer